Key Points:
- The rising-tone chorus waves are generated in a dipole magnetic field with a 2-D gcPIC simulation for the first time
- Whistler waves are excited around the magnetic equator and propagate almost along the background magnetic field
- When whistler waves propagate toward high latitudes, their wave normal angles increase with the growth of the latitude

Supporting Information:
- Supporting Information S1
- Data Set S1
- Data Set S2

Correspondence to:
Q. Lu, and X. Wang,
qmlu@ustc.edu.cn
xywang@physics.auburn.edu

Two-Dimensional gcPIC Simulation of Rising-Tone Chorus Waves in a Dipole Magnetic Field

Quanming Lu[1,2] (iD), Yangguang Ke[1,2] (iD), Xueyi Wang[3] (iD), Kaijun Liu[4] (iD), Xinliang Gao[1,2] (iD), Lunjin Chen[5] (iD), and Shui Wang[1,2]

[1]CAS Key Laboratory of Geospace Environment, Department of Geophysics and Planetary Science, University of Science and Technology of China, Hefei, China, [2]CAS Center for Excellence in Comparative Planetology, Hefei, China, [3]Physics Department, Auburn University, Auburn, AL, USA, [4]Department of Earth and Space Sciences, Southern University of Science and Technology, Shenzhen, China, [5]Department of Physics, University of Texas at Dallas, Richardson, TX, USA

Abstract Rising-tone chorus waves have already been successfully produced in a mirror magnetic field with the use of one- and two-dimensional particle-in-cell (PIC) simulations. However, in reality, the background magnetic field in the inner Earth's magnetosphere is a dipole magnetic field, unlike symmetric mirror fields. In this paper, with the two-dimensional (2-D) general curvilinear PIC (gcPIC) code, we investigate the generation of rising-tone chorus waves in the dipole magnetic field configuration. The plasma consists of three components: immobile ions, cold background, and hot electrons. In order to save computational resource, the topology of the magnetic field is roughly equal to that at $L = 0.6$ R_E, although the plasma parameters corresponding to those at $L = 6$ R_E (R_E is the Earth's radius) are used. Whistler mode waves are first excited around the magnetic equator by the hot electrons with a temperature anisotropy. The excited whistler mode waves propagate almost parallel and antiparallel to the background magnetic field in their source region, which is limited at $|\lambda| \leq 3°$ (where λ is the magnetic latitude). When the waves leave from the source region and propagate toward high latitudes, both their amplitude and wave normal angle become larger. However, the group velocity of the waves is directed toward high latitudes almost along the magnetic field. During such a process, the waves have a frequency chirping, as shown by a rising tone in the frequency-time spectrogram. To our best knowledge, it is for the first time that rising-tone chorus are generated in a dipole magnetic field with a PIC simulation.

1. Introduction

Whistler mode waves, which play a pivotal role in controlling electron dynamics in the radiation belt through pitch angle and energy scattering, are the most fascinating plasma waves in the Earth's magnetosphere (Bortnik & Thorne, 2007; Horne et al., 2003; Summers et al., 2007; Thorne, 2010). Satellite observations have shown that these waves generally propagate along the magnetic field (Santolik et al., 2014; Taubenschuss et al., 2016) and have a frequency range from 0.1 to $0.8f_{ce}$ (where f_{ce} is the equatorial electron gyrofrequency; Burtis & Helliwell, 1969; Li et al., 2012; Meredith et al., 2001; Tsurutani & Smith, 1974, 1977). They not only are the primary mechanism to produce relativistic electrons in the radiation belt (e.g., Horne et al., 2005; Meredith et al., 2001; Summers et al., 1998; Thorne et al., 2013; Xiao et al., 2009) but also can lead to the enhancement of electron precipitation into the Earth's atmosphere (e.g., Lam et al., 2010; Lorentzen et al., 2001; Ni et al., 2008, 2014, 2016; Thorne et al., 2005, 2010).

Whistler mode waves in the radiation belt are considered to be originated around the magnetic equator (Lauben et al., 2002; LeDocq et al., 1998; Li et al., 2009; Santolik et al., 2005) and excited by anisotropic electrons, which are injected from the magnetotail (Kennel & Petschek, 1966; Tsurutani & Smith, 1977). When leaving from the equatorial region and propagating toward high latitudes, they usually exhibit rising or falling tones in the frequency-time spectrogram, which are known as chorus waves (Cornilleau-Wehrlin et al., 1978; Gao et al., 2014; Koons, 1981; Li et al., 2012; Pope, 1963; Santolik et al., 2009). Nonlinear interactions between resonant electrons and a coherent whistler mode wave are believed to be the reason for the formation of the frequency chirping (Gao et al., 2016; Nunn, 1974; Nunn et al., 1997; Omura & Matsumoto, 1982; Omura & Summers, 2006). Omura et al. (2008) found that the trapping of resonant electrons by whistler mode waves results in an electromagnetic electron hole in the wave phase space. A resonant current is

then formed when the background magnetic field is inhomogeneous, and chorus waves with a rising frequency are at last generated.

Particle-in-cell (PIC) simulations provide a powerful tool to study nonlinear interactions between resonant electrons and whistler mode waves and the consequential generation of chorus waves with a frequency chirping. By performing one-dimensional (1-D) PIC simulations in a mirror magnetic field, Hikishima and Omura (2012) revealed the formation of electromagnetic electron holes due to the nonlinear trapping of resonant electrons by whistler mode waves, and then rising-tone chorus waves are generated. The results are consistent with the prediction by Omura et al. (2008). The optimum condition to generate chorus waves is also given in the simulations, and the larger spatial inhomogeneity of the background mirror field is found to increase the amplitude threshold to generate chorus waves. These predictions from 1-D PIC simulations are later supported by satellite observations (Gao et al., 2014). However, all these simulations, which exhibited the generation of rising-tone chorus waves, were performed in a one-dimensional mirror field (Katoh & Omura, 2006; Tao, 2014). Recently, Ke et al. (2017) studied the generation of chorus waves in a mirror magnetic field with a two-dimensional (2-D) PIC simulation. They found that the wave normal angle is smaller than 25°, and it becomes larger when the waves propagate toward the higher latitude regions. However, in reality, the background magnetic field in the radiation belt is a dipole field, rather than a mirror field that is symmetric about the central field line. In this paper, with a two-dimensional general curvilinear PIC (gcPIC) code, for the first time we study the generation of rising-tone chorus waves in a dipole magnetic field.

2. Simulation Model

In this paper, a 2-D gcPIC simulation code is used to study the generation of rising-tone chorus waves in a dipole magnetic field. In the simulation, electrons consist of cold and hot electrons, while ions are assumed to be immobile since the ion cyclotron frequency is much less than the frequency of the excited whistler mode waves. The background cold electrons are treated as a fluid to reduce computational costs, while hot electrons are modeled as particles including the relativistic effect. The motions of cold electrons are controlled by the following fluid equations:

$$\frac{\partial n_c}{\partial t} = -\nabla \cdot (n_c \mathbf{V}_c), \tag{1}$$

$$\frac{\partial \mathbf{V}_c}{\partial t} = -(\mathbf{V}_c \cdot \nabla)\mathbf{V}_c + \frac{q_e}{m_e}(\mathbf{E} + \mathbf{V}_c \times \mathbf{B}), \tag{2}$$

$$\mathbf{J}_c = q_e n_c \mathbf{V}_c, \tag{3}$$

where n_c, $\mathbf{V}_c$, and $\mathbf{J}_c$ are the number density, bulk velocity, and current density of cold electrons. q_e is the electron charge, $\mathbf{B}$ and $\mathbf{E}$ are the magnetic and electric fields.

The motions of hot electrons are governed by the Lorentz force:

$$\frac{\mathrm{d}(\gamma \mathbf{v}_h)}{\mathrm{d}t} = \frac{q_e}{m_e}(\mathbf{E} + \mathbf{v}_h \times \mathbf{B}), \tag{4}$$

where $\mathbf{v}_h$ is the particle velocity of hot electrons and m_e is the electron mass. $\gamma = 1/\sqrt{1-(|\mathbf{v}_h|/c)^2}$ is the Lorentz factor (here c is the light speed in vacuum).

The total current density can be calculated by

$$\mathbf{J} = \mathbf{J}_c + q_e n_h \mathbf{V}_h, \tag{5}$$

where n_h and $\mathbf{V}_h$ are the number density and the bulk velocity of hot electrons, which can be calculated after we know the velocity and location of each individual hot electron.

The magnetic and electric fields are updated by solving Maxwell equations:

$$\frac{\partial \mathbf{E}}{\partial t} = \frac{1}{\mu_0 \varepsilon_0} \nabla \times \mathbf{B} - \frac{1}{\varepsilon_0} \mathbf{J}, \tag{6}$$

$$\frac{\partial \mathbf{B}}{\partial t} = -\nabla \times \mathbf{E}, \tag{7}$$

$$\nabla \cdot \mathbf{B} = 0, \tag{8}$$

$$\nabla \cdot E = \frac{\rho}{\varepsilon_0}, \tag{9}$$

where ρ is the charge density.

The dipole field is used as the background magnetic field $\mathbf{B}_0$ in our simulation system. A modified 2-D dipole coordinate system (p,q) is used in our simulation, which is based on the standard 2-D dipole coordinates (μ, χ). For the standard dipole coordinate system,

$$\mu = -\frac{\sin\lambda}{r^2}, \tag{10}$$

$$\chi = \frac{\cos^2\lambda}{r} = \frac{1}{L}, \tag{11}$$

where r is the distance to the Earth's center, λ is the latitude, and L is the distance of the field line of interest to the Earth's center at the magnetic equator. The modified two-dimensional dipole coordinate system is defined as

$$p = \frac{1}{\chi} = L, \tag{12}$$

$$q = \left(\frac{\mu}{2a} + \sqrt{\left(\frac{\mu}{2a}\right)^2 + \left(\frac{b}{3a}\right)^3} \right)^{\frac{1}{3}} + \left(\frac{\mu}{2a} - \sqrt{\left(\frac{\mu}{2a}\right)^2 + \left(\frac{b}{3a}\right)^3} \right)^{\frac{1}{3}}, \tag{13}$$

where a and b are two constants, which are assumed to be $a = 12/L_0^2$ (where L_0 is the middle L value in the simulation domain) and $b = 1/L_0^2$, respectively. It should be noted that the modified two-dimensional dipole coordinate system used in the paper is an orthogonal one.

Initially, the cold electrons are distributed uniformly in the simulation domain. The velocity distribution of hot electrons is assumed to be bi-Maxwellian distribution with the perpendicular temperature larger than the parallel one. The hot electrons are initialized with a uniform parallel (perpendicular) temperature $T_{\parallel\mathrm{eq}}$ ($T_{\perp\mathrm{eq}}$) and number density $n_{h\mathrm{eq}}$ at the magnetic equator ($q = 0$). Then, according to parallel force balance (Chan et al., 1994), the hot electron pressure can be given by

$$p_\parallel = \frac{n_{h\mathrm{eq}} T_{\parallel\mathrm{eq}}}{\zeta}, \text{ and } p_\perp = \frac{n_{h\mathrm{eq}} T_{\perp\mathrm{eq}}}{\zeta^2}, \tag{14}$$

where $\zeta = 1 + (T_{\perp\mathrm{eq}}/T_{\parallel\mathrm{eq}} - 1)(1 - B_{0\mathrm{eq}}/B_0)$, B_0 is the strength of the background magnetic field, and $B_{0\mathrm{eq}}$ is its value at the equator. Based on conservation of energy and the magnetic moment, the number density of hot electrons is derived to be

$$n_h = n_{h\mathrm{eq}}/\zeta, \tag{15}$$

Therefore, the parallel and perpendicular temperatures of hot electrons off the equator are

$$T_\parallel = T_{\parallel\mathrm{eq}}, \text{ and } T_\perp = T_{\perp\mathrm{eq}}/\zeta, \tag{16}$$

At last, the distribution function of hot electrons can be described as
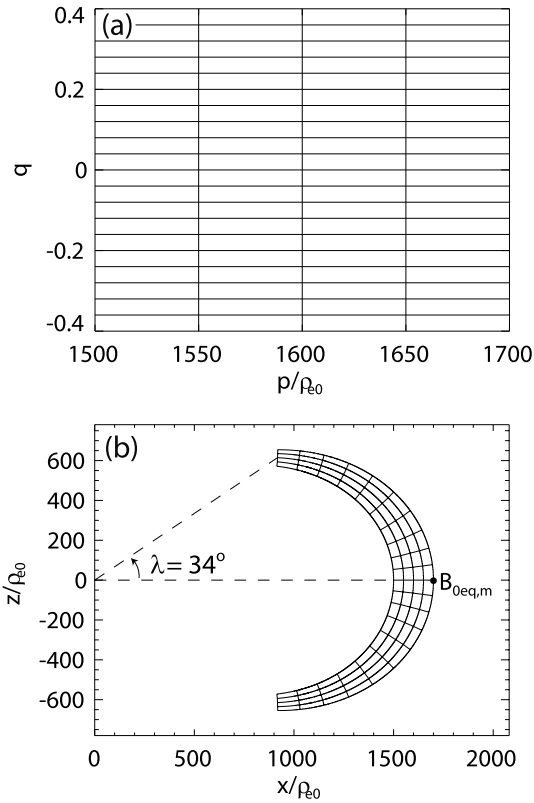
Figure 1. Mapping of the simulation domain between (a) the modified dipole coordinates (p,q) and (b) the Cartesian coordinates (x,z). The vertical lines p = constant in Figure 1a correspond to the dipole field lines in Figure 1b. The latitude λ is 34° for the middle field line in the simulation domain. The background magnetic field at the outer boundary of the equator is $B_{0eq,m}$.

$$f(v_{h\parallel}, v_{h\perp}) = \frac{1}{(2\pi)^{3/2} w_{\parallel eq} w_{\perp eq}^2/\zeta} \exp\left(-\frac{v_{h\parallel}^2}{2w_{h\parallel}^2} - \frac{v_{h\perp}^2}{2w_{h\perp}^2/\zeta}\right), \quad (17)$$

where $w_{\parallel eq}$ and $w_{\perp eq}$ are the parallel and perpendicular thermal velocities of hot electrons at the equator, respectively.

The parameters used in the simulation are the follows: the ratio of the number density of hot electrons to that of cold electrons at the equator is $n_{heq}/n_{c0} = 0.01$, the ratio of cold electron plasma frequency to electron gyrofrequency is $\omega_{pe}/\Omega_{e0} = 5$ (where $\omega_{pe} = \sqrt{n_{c0}e^2/m_e\varepsilon_0}$ is the cold electron plasma frequency, and $\Omega_{e0} = eB_{0eq,m}/m_e$ is the electron gyrofrequency defined on the background magnetic field at the outer boundary of the equator $B_{0eq,m}$), the temperature anisotropy of hot electrons at the equator is $T_{\perp eq}/T_{\parallel eq} = 6$, and the parallel plasma beta at the outer boundary of the equator is $\beta_{\parallel eq,m} = n_{heq}T_{\parallel eq}/\left(B_{0eq,m}^2/2\mu_0\right) = 0.01$. The simulation domain is a rectangle in (p,q) space, which is divided into $n_p \times n_q = 64 \times 4,000$ uniform grids. The mapping of the simulation domain between (a) the modified dipole coordinates (p,q) and (b) the Cartesian coordinates (x,z) is shown in Figure 1. The vertical lines p=constant in Figure 1a correspond to the dipole field lines in Figure 1b. In the inner boundary $p = 1,500\rho_{e0}$ (where $\rho_{e0} = w_{\parallel eq}/\Omega_{e0}$), and the value of p in the outer boundary is $1,700\rho_{e0}$. According to the typical electron number density, electron temperature, and strength of magnetic field at $L = 6R_E$ (R_E is the Earth's radius), we can estimate that the topology of the magnetic field in the simulation is roughly equal to that at $L = 0.6R_E$. In this way, we can reduce the computation costs. In the simulation, we choose the range of q as $-0.4 \leq q \leq 0.4$ in the modified dipole coordinate, corresponding to a rough latitude range of $-34° \leq \lambda \leq 34°$. The grid spacing along the field lines has the maximum value $0.68\rho_{e0}$ and the minimum value $0.26\rho_{e0}$. Across the field lines, the grid spacing has the maximum value $3.13\rho_{e0}$ at the equator and the minimum value $1.28\rho_{e0}$ at the highest latitude. The time step is $\Omega_{e0}\Delta t = 0.02$. On average, there are about 1,000 superparticles per cell, and totally about 2.56×10^8 particles are used in the simulation.

There are two types of boundary conditions in our simulation. Absorbing boundary conditions are used for waves, and reflecting boundary conditions are employed for particles. For the reflecting boundary conditions, the particles are reflected in a way described in Hu and Denton (2009).

3. Simulation Results

Figure 2 shows the initial distribution of number density and temperature anisotropy of hot electrons. Both the temperature anisotropy and density reach their maximum values at the equator, which gradually decrease toward the polar region. In general, such temperature anisotropy can excite whistler mode waves. Figure 3 shows spatial profiles of the perpendicular magnetic fluctuations $B_{\perp 1}$ (the component perpendicular to the simulation plane) at $\Omega_{e0}t = $ (a) 400, (b) 600, (c) 800, and (d) 1,000, respectively. The magnetic fluctuations $B_{\perp 1}$ begin to appear around $\Omega_{e0}t = 400$, which are concentrated around the magnetic equator. Then, these fluctuations propagate toward higher latitudes, and their amplitude first increases and then saturates after they reach a sufficiently high magnetic latitude. This can be identified more clearly if we follow the same wave pack in Figures 3b, 3c, and 3d (circled by the while solid lines in the figure). We can also find that this wave packet moves almost along the same magnetic field line (the black line denoted by "J"), although the oblique wave normal with respect to the field line can be seen at high latitudes in Figures 3c and 3d (also see Movies S1 and S2). The characteristics of the magnetic fluctuations will be described in detail later.

In order to verify that the excited magnetic fluctuations belong to whistler mode waves, we calculate the power spectra of the magnetic fluctuation $B_{\perp 1}$ in the $(\omega, k_{\parallel})$ space by spatial and temporal Fourier
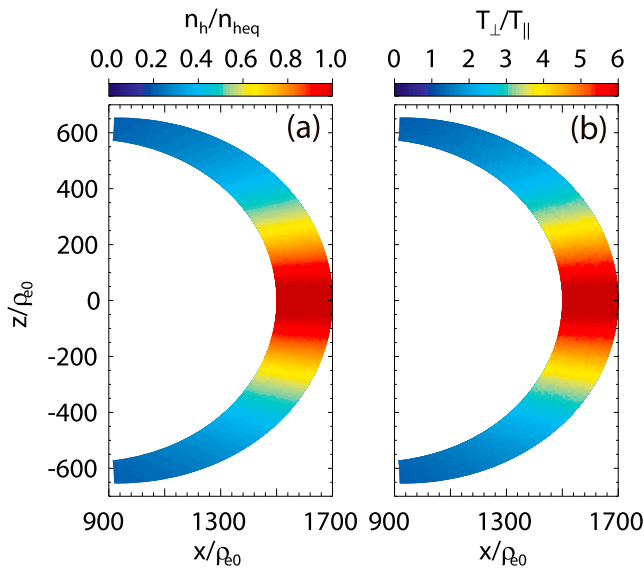
Figure 2. (a) Initial distribution of the hot electron number density n_h/n_{heq} and (b) the anisotropy of hot electrons $T_\perp/T_\parallel$ in the simulation domain.

transformation of the magnetic fluctuation $B_{\perp 1}$ along the magnetic field line $L = 1{,}600\rho_{e0}$ with $-1\ ^\circ \leq \lambda \leq 1°$, and the time period is $300 \leq \Omega_{e0}t \leq 555$. During this time period, the magnetic fluctuations just begin to appear around the magnetic equator. We expect the linear theory should work near the equatorial region because the wave amplitude is small and inhomogeneity is small, as demonstrated below. The power spectra in the $(\omega, k_\parallel)$ space obtained from the simulation are shown in Figure 4, and the dispersion relation of whistler mode waves based on the linear theory, which is calculated with the WHAMP software package (Ronnmark, 1982), is also plotted in the figure for comparison. When we calculate the dispersion relation based on the linear theory, we use the plasma parameters at the corresponding magnetic equator and assume that the plasma is uniform. The calculated power spectra of the magnetic fluctuations from the simulation lie on the dispersion relation of the whistler mode waves, which confirms that the magnetic fluctuations in the simulation belong to whistler mode waves excited by the anisotropic hot electrons. Also, we compare the maximum growth rate from the simulation with that from the linear theory. In the simulation, the maximum growth rate is about $1.4 \times 10^{-2}\Omega_{e0}$ at $(\omega, k) = (0.4\Omega_{e0}, 0.68\rho_{e0})$, while the linear theory predicts that the maximum growth rate is $1.3 \times 10^{-2}\Omega_{e0}$ at $(\omega, k) = (0.44\Omega_{e0}, 0.76\rho_{e0})$. With the excitation of whistler mode waves, we observed the typical relaxation of the electron temperature anisotropy around the equator (not shown).
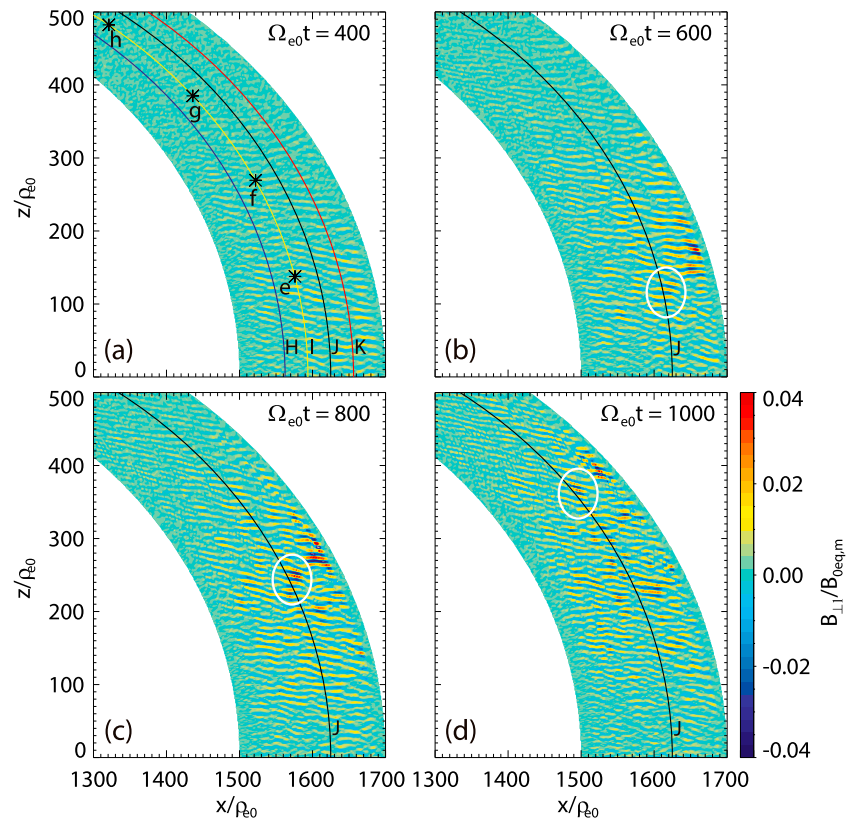
Figure 3. Spatial profiles of the perpendicular magnetic fluctuations $B_{\perp 1}/B_{0eq,m}$ at $\Omega_{e0}t =$ (a) 400, (b) 600, (c) 800, and (d) 1,000, respectively. These different-colored curve lines represent different magnetic field lines denoted by "H," "I," "J," and "K." And four locations (marked by e–h) at $\lambda = 5°$, $10°$, $15°$, and $20°$ along the field line "I" are denoted by symbols "*". The same wave packets at $\Omega_{e0}t = 600$, 800, and 1,000 are circled by the white solid lines.
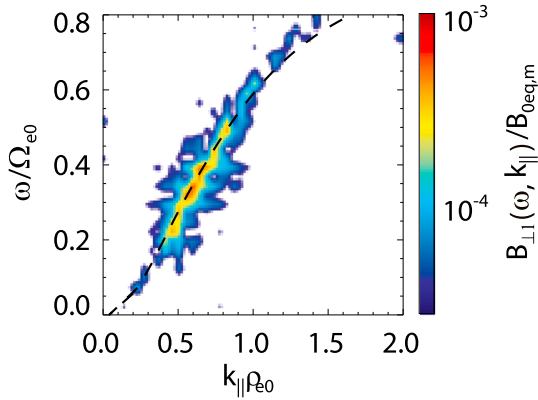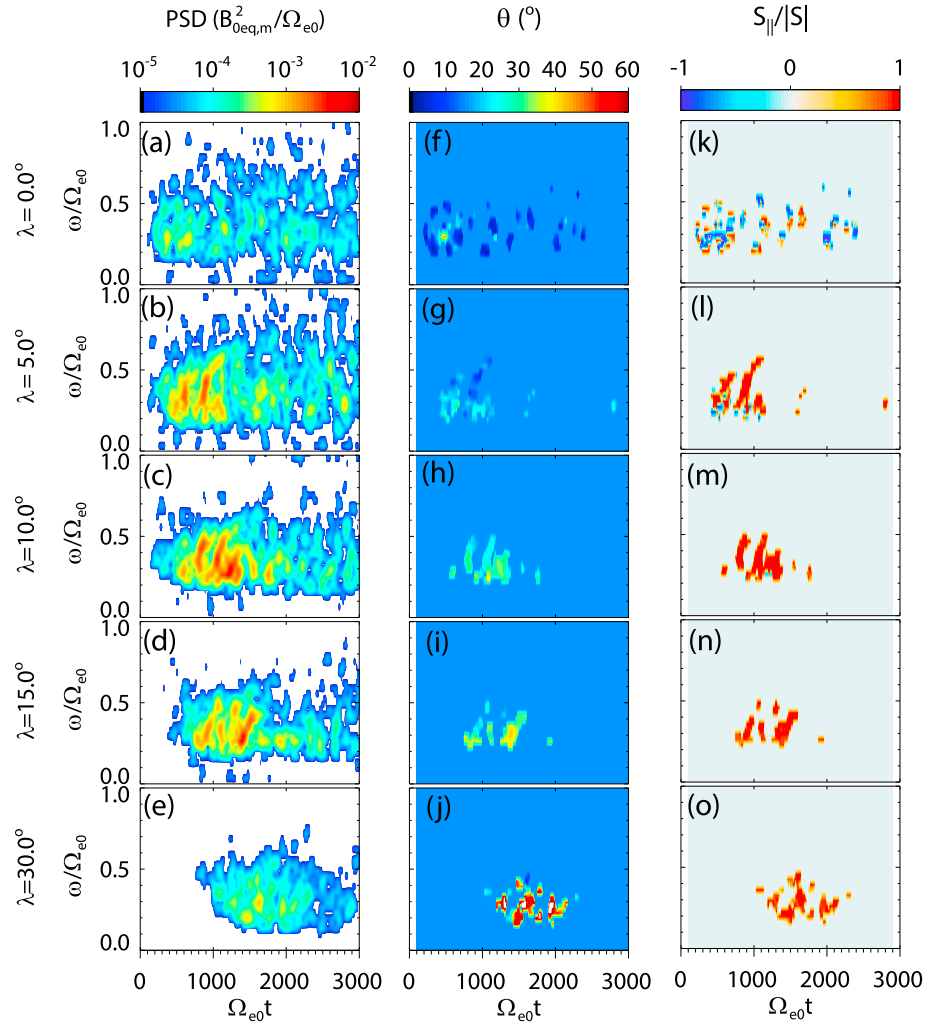
Figure 4. The power spectra of magnetic fluctuations $B_{\perp 1}(\omega, k_{\parallel})/B_{0\mathrm{eq},m}$ by Fourier analysis of $B_{\perp 1}$ in the region ($L = 1{,}600\rho_{e0}, -1° \leq \lambda \leq 1°$) during the time period $300 \leq \Omega_{e0}t \leq 555$. The dotted line denotes the $\omega - k_{\parallel}$ dispersion relation of whistler mode waves under the plasma condition at $L = 1{,}600\rho_{e0}$ and $\lambda = 0$, which is calculated with the WHAMP software package.

Figure 5 exhibits (a) the frequency-time spectrogram of the magnetic power spectra density (PSD), (b) the wave normal angle θ, and (c) the parallel component of Poynting vector $\mathbf{S}_{\parallel}/|\mathbf{S}|$ of the excited whistler mode waves at five different locations $\lambda = 0°, 5°, 10°, 15°,$ and $30°$ along the same magnetic field line denoted by "I" in Figure 3a. The wave normal angle is estimated by the singular value decomposition method based on magnetic field waveforms (Santolik et al., 2003). Around the magnetic equator (Figures 5f and 5g), the excited whistler mode waves propagate quasi-parallel to the background magnetic field, and the wave normal angles of most whistler modes are smaller than 20°. The corresponding parallel component of Poynting vector $\mathbf{S}_{\parallel}/|\mathbf{S}|$ can vary from -1.0 to 1.0 at the equator (Figure 5k), which means that the waves propagate both parallel and antiparallel to the background magnetic field. The wave normal angles become larger and larger when they propagate away from the equator (Figures 5h–5j). The wave normal angles can attain about 50° at $\lambda = 30°$ (Figure 5j). For the magnetic latitude λ larger than about 3°, the parallel components of Poynting vector $\mathbf{S}_{\parallel}/|\mathbf{S}|$ become close to 1.0 (Figures 5i–5o), meaning the wave energy propagates toward the polar region almost along the background magnetic field. This is consistent with the evolution of the wave pack identified in Figure 3. From the frequency-time spectrogram of the PSD, we can find that the whistler mode waves have a frequency chirping (increasing frequency with the time) when the magnetic latitude λ is larger than about 3° (Figures 5b–5d). Such frequency chirping is one of the key characteristics of rising-tone chorus waves, which have been widely observed by satellites in the magnetosphere (e.g., Gao et al., 2014; Li et al., 2012; Santolik et al., 2009) and have been also produced by one- or two-dimensional PIC simulations in a mirror magnetic field (Hikishima & Omura, 2012; Ke et al., 2017; Tao, 2014). Nonetheless, from the simulation, we also find that there is no clear frequency chirping for the magnetic latitude λ larger than 25° (Figure 5e).

The characteristics of rising-tone chorus waves are further examined in Figures 6 and 7. Figure 6 shows the average values of (a) the intensity of the fluctuating magnetic field $\left\langle B_w^2/B_{0\mathrm{eq},m}^2 \right\rangle$, (b) the wave normal angle $\langle \theta \rangle$, and (c) the parallel component of Poynting vector $\langle \mathbf{S}_{\parallel}/|\mathbf{S}| \rangle$ as a function of latitudes along the magnetic field lines denoted by "H," ",I" "J," and "K" in Figure 3a. Here, $B_w^2 = \delta B_{\parallel}^2 + B_{\perp 1}^2 + B_{\perp 2}^2$, where $\delta B_{\parallel}$ and $B_{\perp 2}$ are the parallel and another perpendicular component of magnetic fluctuations. These average values are calculated over the time period $0 \leq \Omega_{e0}t \leq 3{,}000$. Besides, $\langle \theta \rangle$ and $\langle \mathbf{S}_{\parallel}/|\mathbf{S}| \rangle$ are average values weighted by PSD (ω, t). When the whistler mode waves propagate away from the equator, their intensity first enhances and then decays, reaching a maximum value around $\lambda \approx 10°$ (Figure 6a). But their wave normal angles increase with the growth of the latitude (Figure 6b). Also, the average parallel component of Poynting vector $\langle \mathbf{S}_{\parallel}/|\mathbf{S}| \rangle$ is small at the equator due to both parallel and antiparallel whistler mode waves (Figure 5k) but increases rapidly around $\lambda \approx 3°$. Then it increases gradually and reaches a saturation value close to 1.0 (Figure 6c). Therefore, in the region with $\lambda \geq 3°$, the group velocity of the waves is directed toward the polar region almost along the background magnetic field.
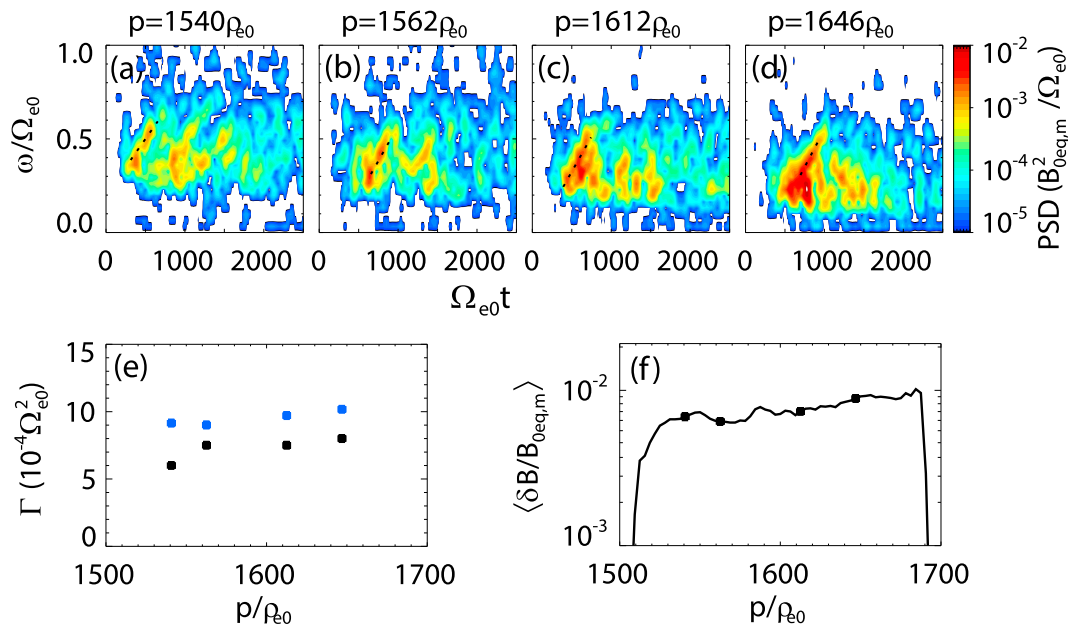
In Figures 7a–7d, we plot the frequency-time spectrogram of the magnetic PSD at $\lambda = -6°$ along the magnetic field lines at $p = 1{,}540\rho_{e0}, 1{,}562\rho_{e0}, 1{,}612\rho_{e0},$ and $1{,}646\rho_{e0}$, respectively. The frequency chirping with a rising tone can be clearly identified. In the figure, we use the dotted line to fit the chorus elements with clear rising-tone signature by the linear least square method, and the slope of the dotted line is evaluated as the chirping rate Γ. The chirping rate Γ tends to increase with p. In Figure 7e, we show the calculated frequency chirping rate Γ (black dots) at $\lambda = -6°$ along the magnetic field lines at $p = 1{,}540\rho_{e0}, 1{,}562\rho_{e0}, 1{,}612\rho_{e0},$ and $1{,}646\rho_{e0}$, respectively. The chirping rates increase from about $6.0\times10^{-4}\Omega_{e0}^2$ at $p = 1{,}540\rho_{e0}$ to about 8.0×10^{-4} Ω_{e0}^2 at $p = 1{,}646\rho_{e0}$. In Figure 7f, we show the averaged wave amplitude $\langle \delta B/B_{0\mathrm{eq},m} \rangle$ over $\Omega_{e0}t = 0 - 1{,}500$ at equator as a function of distances from the Earth's center. The wave amplitude increases with the distance. According to equation (50) of Omura et al. (2008), we can also calculate the theoretical prediction of the chirping rate based on the wave amplitude (black dots in Figure 7f), which is plotted in Figure 7e. The theoretical prediction is consistent with the simulation results.

Figure 5. Frequency-time spectrogram of (a–e) the power spectral density (PSD) of magnetic fluctuations, (f–j) wave normal angle θ, and (k–o) parallel component of Poynting vector $\mathbf{S}_\parallel/|\mathbf{S}|$ of the excited whistler mode waves at five different locations $\lambda = 0°$, 5°, 10°, 15°, and 30° along the same field line denoted by "I" in Figure 3a.
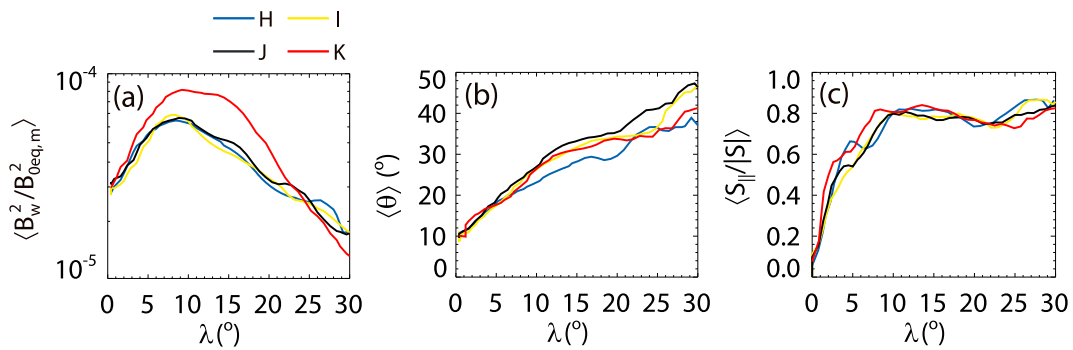
Figure 6. The average values of (a) the intensity of the fluctuating magnetic field $\left\langle B_w^2/B_{0eq,m}^2 \right\rangle$ (here $B_w^2 = \delta B_\parallel^2 + B_{\perp 1}^2 + B_{\perp 2}^2$), (b) wave normal angle $\langle\theta\rangle$, and (c) parallel component of Poynting vector $\langle\mathbf{S}_\parallel/|\mathbf{S}|\rangle$ of whistler mode waves versus the latitude λ along the magnetic field lines denoted by "H," "I," "J," and "K" in Figure 3a. Besides, $\langle\theta\rangle$ and $\langle\mathbf{S}_\parallel/|\mathbf{S}|\rangle$ are average values weighted by power spectra density (ω, t). Here, the average values are calculated over the time period $\Omega_{e0}t = 0 - 3,000$.

Figure 7. (a–d) Frequency-time spectrogram of the magnetic power spectra density (PSD) at $\lambda = -6°$ along field lines $p = 1{,}540\rho_{e0}$, $1{,}562\rho_{e0}$, $1{,}612\rho_{e0}$, and $1{,}646\rho_{e0}$, respectively. The clear chorus element is fitted by the dotted line by using the linear least squares method, and the frequency chirping rate Γ is obtained from the slope of the dotted line. (e) Distribution of the chirping rates Γ over different field lines. The black dots represent the chirping rates calculated from our simulation (Figures 7a–7d). The blue dots are theoretical predictions of the chirping rates based on equation (50) of Omura et al. (2008). When we use this equation, (k,ω) are the values when wave mode at equator obtains the maximum growth rate based on the linear theory, and the amplitude of whistler mode waves is the averaged amplitude in Figure 7f (denoted by black dots). (f) The averaged amplitude $\langle \delta B/B_{0eq,m} \rangle$ of the whistler mode waves integrated over $\omega = 0.1\Omega_{e0}$ to $0.5\Omega_{e0}$ over $\Omega_{e0}t = 0 - 1{,}500$ at equator as a function of distances from the Earth's center.

4. Conclusions and Discussion

In this paper, with a two-dimensional gcPIC simulation code, we investigate the generation of rising-tone chorus waves in a dipole magnetic field. The results show that whistler mode waves are first excited by an anisotropic electron distribution around the magnetic equator, with coexisting parallel and antiparallel propagation along the background magnetic field. After they leave away from the source region, the waves can only propagate toward the polar region when the magnetic latitude λ is larger than about 3°. Their amplitude and wave normal angle become larger during the poleward propagation, and the intensity saturates around $\lambda \approx 10°$. However, although the phase velocity of the waves is oblique to the background magnetic field, the group velocity is almost along the background magnetic field. Furthermore, the waves have a frequency chirping with a rising tone over a limited latitude range. The chirping appears when the magnetic latitude λ is larger than about 3°, while the chirping starts to disappear when the magnetic latitude λ is around 25°.

Rising-tone chorus waves have been studied by 1-D and 2-D PIC simulations in a mirror magnetic field. However, in reality, the Earth's inner magnetosphere has a dipole magnetic field. Wu et al. (2015) has also performed 2-D hybrid simulations to study the generation of whistler mode waves in a dipole magnetic field, but these waves have no obvious frequency chirping. To our best knowledge, our simulation for the first time reproduces rising-tone chorus waves in a 2-D dipole magnetic field. The whistler mode waves are first excited by an anisotropic electron distribution around the magnetic equator ($|\lambda| \leq 3°$,). Such latitudinal range is consistent with previous satellite observations (Santolik et al., 2004; Teng et al., 2018). After the whistler mode waves leave the source region and obtain a sufficiently large amplitude, they begin to have a frequency chirping and evolve into rising-tone chorus waves. Rising-tone chorus waves have been thoroughly studied by THEMIS and Van Allen Probes (e.g., Gao et al., 2014; Li et al., 2009, 2011, 2012, 2016, 2017). Our simulation also find that the frequency chirping will disappear when the waves reach high-latitude region. This is consistent with satellite observations (Tsurutani & Smith, 1977), which show statistically that chorus waves only exist in the lower latitude region of the magnetotail. We also notice that several conjugate ground-spacecraft observations of rising-tone chorus waves indicated that chorus waves can propagate to the high latitude region (Demekhov et al., 2017; Manninen et al., 2012). These chorus

events can be accounted for by propagation due to a density duct. As described by Demekhov et al. (2017), when chorus waves were observed by satellite, the satellite was passing a duct with a density enhancement with a transverse scale about 600 km, and the chorus waves propagate almost parallel to the background magnetic field in the duct to the ground. Because of the parallel propagation, wave damping is also reduced, which makes high-latitude chorus possible. Because the present satellites, like THEMIS and Van Allen Probe, only cross the low-latitude region of the inner magnetosphere, this prediction needs to be verified using the plasma wave data obtained from Arase satellite with a higher inclination than that of THEMIS and Van Allen Probe in the future.

Our simulation describes how rising-tone chorus waves propagate toward the polar region: The group velocity or the Poynting vector is almost directed toward the polar region along the background magnetic field, although the wave normal angles tend to increase during their poleward propagation. Both satellite observations and ray tracing calculations have found that the wave normal angles of chorus waves become larger in the higher latitude region (Agapitov et al., 2018; Artemyev et al., 2016; Bortnik et al., 2011; Breuillard et al., 2012; Chen et al., 2012, 2013). Based on 6 years of THEMIS observations, Taubenschuss et al. (2016) found that Poynting vectors of whistler mode waves are almost parallel to the background magnetic field. Our simulation also shows that as latitude increases, the intensity of chorus waves first enhances and then decays, with a peak value reached around $\lambda \approx 10°$. This is consistent with the synthetic observation study of chorus waves based on combined Van Allen Probes and Cluster data by Agapitov et al. (2018). In their study, chorus wave intensity has a peak between $\lambda \approx 5°$ and 15° during periods of quiet or moderate activity at $L = 4 - 6R_E$ on the dawnside and decreases by a factor of ~5–10 at $\lambda \approx 30°$. The attenuation of chorus waves in the high latitude is considered to be caused by Landau damping due to increasing wave normal angle (Chen et al., 2013). Although our simulation provides consistent results on the propagation of chorus waves in the inner magnetosphere, extra caution should be excised when interpreting magnetic latitude in the simulation and making quantitative comparison with that in the actual magnetospheric region of chorus generation, because the topology of the magnetic field roughly around $L = 0.6R_E$ is used in the simulation in order to reduce computational cost.

References

Agapitov, O., Mourenas, D., Artemyev, A., Mozer, F. S., Hospodarsky, G., Bonnell, J., & Krasnoselskikh, V. (2018). Synthetic empirical chorus wave normal model from combined Van Allen Probes and Cluster statistics. *Journal of Geophysical Research: Space Physics*, *123*, 297–314. https://doi.org/10.1002/2017JA024843

Artemyev, A., Agapitov, O., Mourenas, D., Krasnoselskikh, V., Shastun, V., & Mozer, F. (2016). Oblique whistler-mode waves in the Earth's inner magnetosphere: Energy distribution, origins, and role in radiation belt dynamics. *Space Science Reviews*, *200*(1-4), 261–355. https://doi.org/10.1007/s11214-016-0252-5

Bortnik, J., Chen, L. J., Li, W., Thorne, R. M., & Hornes, R. B. (2011). Modeling the evolution of chorus waves into plasmaspheric hiss. *Journal of Geophysical Research*, *116*, A08221. https://doi.org/10.1029/2011JA016499

Bortnik, J., & Thorne, R. M. (2007). The dual role of ELF/VLF chorus waves in the acceleration and precipitation of radiation belt electrons. *Journal of Atmospheric and Solar - Terrestrial Physics*, *69*(3), 378–386. https://doi.org/10.1016/j.jastp.2006.05.030

Breuillard, H., Zaliznyak, Y., Krasnoselskikh, V., Agapitov, O., Artemyev, A., & Rolland, G. (2012). Chorus wave-normal statistics in the Earth's radiation belts from ray tracing technique. *Annales de Geophysique*, *30*(8), 1223–1233. https://doi.org/10.5194/angeo-30-1223-2012

Burtis, W. J., & Helliwell, R. A. (1969). Banded chorus—A new type of VLF radiation observed in the magnetosphere by OGO 1 and OGO 3. *Journal of Geophysical Research*, *74*(11), 3002–3010. https://doi.org/10.1029/JA074i011p03002

Chan, A. A., Xia, M., & Chen, L. (1994). Anisotropic Alfvén-ballooning modes in Earth's magnetosphere. *Journal of Geophysical Research*, *99*(A9), 17,351–17,366. https://doi.org/10.1029/93JA03353

Chen, L. J., Bortnik, J., Li, W., Thorne, R. M., & Horne, R. B. (2012). Modeling the properties of plasmaspheric hiss: 2. Dependence on the plasma density distribution. *Journal of Geophysical Research*, *117*, A05202. https://doi.org/10.1029/2011JA017202

Chen, L. J., Thorne, R. M., Li, W., & Bortnik, J. (2013). Modeling the wave normal distribution of chorus waves. *Journal of Geophysical Research: Space Physics*, *118*, 1074–1088. https://doi.org/10.1029/2012JA018343

Cornilleau-Wehrlin, N., Gendrin, R., Lefeuvre, F., Parrot, M., Grard, R., Jones, D., et al. (1978). VLF electromagnetic waves observed onboard GEOS-1. *Space Science Reviews*, *22*(4), 371–382. https://doi.org/10.1007/BF00210874

Demekhov, A. G., Manninen, J., Santolok, O., & Titova, E. E. (2017). Conjugate ground-spacecraft observations of VLF chorus elements. *Geophysical Research Letters*, *44*, 11,735–11,744. https://doi.org/10.1002/2017GL076139

Gao, X. L., Li, W., Thorne, R. M., Bortnik, J., Angelopoulos, V., Lu, Q. M., et al. (2014). New evidence for generation mechanisms of discrete and hiss-like whistler mode waves. *Geophysical Research Letters*, *41*, 4905–4811. https://doi.org/10.1029/2012JA018343

Gao, X. L., Mourenas, D., Li, W., Artemyev, A. V., Lu, Q. M., Tao, X., & Wang, S. (2016). Observational evidence of generation mechanisms for very oblique lower band chorus using THEMIS waveform data. *Journal of Geophysical Research: Space Physics*, *121*, 6732–6748. https://doi.org/10.1002/2016JA022915

Hikishima, M., & Omura, Y. (2012). Particle simulations of whistler-mode rising-tone emissions triggered by waves with different amplitudes. *Journal of Geophysical Research*, *117*, A04226. https://doi.org/10.1029/2011JA017428

Horne, R. B., Glauert, S. A., & Thorne, R. M. (2003). Resonant diffusion of radiation belt electrons by whistler mode chorus. *Geophysical Research Letters*, *30*(9), 1493. https://doi.org/10.1029/2003GL016963

Horne, R. B., Thorne, R. M., Glauert, S. A., Albert, J. M., Meredith, N. P., & Anderson, R. R. (2005). Timescale for radiation belt electron acceleration by whistler mode chorus waves. *Journal of Geophysical Research*, *110*, A03225. https://doi.org/10.1029/2004JA010811

Hu, Y., & Denton, R. E. (2009). Two-dimensional hybrid code simulation of electromagnetic ion cyclotron waves in a dipole magnetic field. *Journal of Geophysical Research*, *114*, A12217. https://doi.org/10.1029/2009JA014570

Katoh, Y., & Omura, Y. (2006). A study of generation mechanism of VLF triggered emission by self-consistent particle code. *Journal of Geophysical Research*, *111*, A12207. https://doi.org/10.1029/2006JA011704

Ke, Y., Gao, X., Lu, Q., Wang, X., & Wang, S. (2017). Generation of risingtone chorus in a two-dimensional mirror field by using the general curvilinear PIC code. *Journal of Geophysical Research: Space Physics*, *122*, 8154–8165. https://doi.org/10.1002/2017JA024178

Kennel, C. F., & Petschek, H. E. (1966). Limit on stable trapped particle fluxes. *Journal of Geophysical Research*, *71*(1), 1–28. https://doi.org/10.1029/JZ071i001p00001

Koons, H. C. (1981). The role of hiss in magnetospheric chorus emissions. *Journal of Geophysical Research*, *86*(A8), 6745–6754. https://doi.org/10.1029/JA086iA08p06745

Lam, M. M., Horne, R. B., Meredith, N. P., Glauert, S. A., Moffat-Griffin, T., & Green, J. C. (2010). Origin of energetic electron precipitation >30 keV into the atmosphere. *Journal of Geophysical Research*, *115*, A00F08. https://doi.org/10.1029/2009JA014619

Lauben, D. S., Inan, U. S., Bell, T. F., & Gurnett, D. A. (2002). Source characteristics of ELF/VLF chorus. *Journal of Geophysical Research*, *107*(A12), 1429. https://doi.org/10.1029/2000JA003019

LeDocq, M. J., Gurnett, D. A., & Hospodarsky, G. B. (1998). Chorus source locations from VLF Poynting flux measurements with the Polar spacecraft. *Geophysical Research Letters*, *25*(21), 4063–4066. https://doi.org/10.1029/1998GL900071

Li, J., Bortnik, J., An, X., Li, W., Thorne, R. M., Zhou, M., et al. (2017). Chorus wave modulation of Langmuir waves in the radiation belts. *Geophysical Research Letters*, *44*, 11,713–11,721. https://doi.org/10.1002/2017GL075877

Li, W., Bortnik, J., Thorne, R. M., & Angelopoulos, V. (2011). Global distribution of wave amplitudes and wave normal angles of chorus waves using THEMIS wave observations. *Journal of Geophysical Research*, *116*, A12205. https://doi.org/10.1029/2011JA017035

Li, W., Santolik, O., Bortnik, J., Thorne, R. M., Kletzing, C. A., Kurth, W. S., & Hospodarsky, G. B. (2016). New chorus wave properties near the equator from Van Allen Probes wave observations. *Geophysical Research Letters*, *43*, 4725–4735. https://doi.org/10.1002/2016GL068780

Li, W., Thorne, R. M., Angelopoulos, V., Bonnell, J. W., McFadden, J. P., Carlson, C. W., et al. (2009). Evaluation of whistler-mode chorus intensification on the nightside during an injection event observed on the THEMIS spacecraft. *Journal of Geophysical Research*, *114*, A00C14. https://doi.org/10.1029/2008JA013554

Li, W., Thorne, R. M., Bortnik, J., Tao, X., & Angelopoulos, V. (2012). Characteristics of hiss-like and discrete whistler mode emissions. *Geophysical Research Letters*, *39*, L18106. https://doi.org/10.1029/2012GL053206

Lorentzen, K. R., Blake, J. B., Inan, U. S., & Bortnik, J. (2001). Observations of relativistic electron microbursts in association with VLF chorus. *Journal of Geophysical Research*, *106*(A4), 6017–6027. https://doi.org/10.1029/2000JA003018

Manninen, J., Kleimenova, N. G., Kozyreva, O. V., Parrot, M., Raita, T., & Turunen, T. (2012). Experimental evidence of the simultaneous occurrence of VLF chorus on the ground in the global azimuthal scale-from pre-midnight to the late morning. *Annales de Geophysique*, *30*(4), 725–732. https://doi.org/10.5194/angeo-30-725-2012

Meredith, N. P., Horne, R. B., & Anderson, R. R. (2001). Substorm dependence of chorus amplitudes: Implications for the acceleration of electrons to relativistic energies. *Journal of Geophysical Research*, *106*(A7), 13,165–13,178. https://doi.org/10.1029/2000JA900156

Ni, B., Bortnik, J., Nishimura, Y., Thorne, R. M., Li, W., Angelopoulos, V., et al. (2014). Chorus wave scattering responsible for the Earth's dayside diffuse auroral precipitation: A detailed case study. *Journal of Geophysical Research: Space Physics*, *119*, 897–908. https://doi.org/10.1002/2013JA019507

Ni, B., Thorne, R. M., Shprits, Y. Y., & Bortnik, J. (2008). Resonant scattering of plasma sheet electrons by whistler-mode chorus: Contribution to diffuse auroral precipitation. *Geophysical Research Letters*, *35*, L11106. https://doi.org/10.1029/2008GL034032

Ni, B., Thorne, R. M., Zhang, X., Bortnik, J., Pu, Z., Xie, L., et al. (2016). Origins of the Earth's diffuse auroral precipitation. *Space Science Reviews*, *200*(1-4), 205–259. https://doi.org/10.1007/s11214-016-0234-7

Nunn, D. (1974). A self-consistent theory of triggered VLF emissions. *Planetary and Space Science*, *22*(3), 349–378. https://doi.org/10.1016/0032-0633(74)90070-1

Nunn, D., Omura, Y., Matsumoto, H., Nagano, I., & Yagitani, S. (1997). The numerical simulation of VLF chorus and discrete emissions observed on the Geotail satellite using a Vlasov code. *Journal of Geophysical Research*, *102*(A12), 27,083–27,097. https://doi.org/10.1029/97JA02518

Omura, Y., Katoh, Y., & Summers, D. (2008). Theory and simulation of the generation of whistler-mode chorus. *Journal of Geophysical Research*, *113*, A04223. https://doi.org/10.1029/2007JA012622

Omura, Y., & Matsumoto, H. (1982). Computer simulations of basic processes of coherent whistler wave-particle interactions in the magnetosphere. *Journal of Geophysical Research*, *87*(A6), 4435–4444. https://doi.org/10.1029/JA087iA06p04435

Omura, Y., & Summers, D. (2006). Dynamics of high-energy electrons interacting with whistler mode chorus emissions in the magnetosphere. *Journal of Geophysical Research*, *111*, A09222. https://doi.org/10.1029/2006JA011600

Pope, J. H. (1963). A high-latitude investigation of the natural very-low-frequency electromagnetic radiation known as chorus. *Journal of Geophysical Research*, *68*(1), 83–99. https://doi.org/10.1029/JZ068i001p00083

Ronnmark, K. (1982). WHAMP: Waves in homogeneous, anisotropic, multicomponent plasmas. Report No. 179, Kiruna Geophysics Institute, Kiruna, Sweden.

Santolik, O., Gurnett, D. A., Pickett, J. S., Chum, J., & Cornilleau-Wehrlin, N. (2009). Oblique propagation of whistler mode waves in the chorus source region. *Journal of Geophysical Research*, *114*, A00F03. https://doi.org/10.1029/2009JA014586

Santolik, O., Gurnett, D. A., Pickett, J. S., Parrot, M., & Cornilleau-Wehrlin, N. (2004). A microscopic and nanoscopic view of storm-time chorus on 31 March 2001. *Geophysical Research Letters*, *31*, L020801. https://doi.org/10.1029/2003GL018757

Santolik, O., Gurnett, D. A., Pickett, J. S., Parrot, M., & Cornilleau-Wehirlin, N. (2005). Central position of the source region of storm-time chorus. *Planetary and Space Science*, *53*, 299–305. https://doi.org/10.1016/j.pss.2004.09.056

Santolik, O., Macúšová, E., Kolmašová, I., Cornilleau-Wehrlin, N., & de Conchy, Y. (2014). Propagation of lower-band whistler-mode waves in the outer Van Allen belt: Systematic analysis of 11 years of multi-component data from the Cluster spacecraft. *Geophysical Research Letters*, *41*, 2729–2737. https://doi.org/10.1002/2014GL059815

Santolik, O., Parrot, M., & Lefeuvre, F. (2003). Singular value decomposition methods for wave propagation analysis. *Radio Science*, *38*(1), 1010. https://doi.org/10.1029/2000RS002523

Summers, D., Ni, B., & Meredith, N. P. (2007). Timescales for radiation belt electron acceleration and loss due to resonant wave-particle interactions: 2. Evaluation for VLF chorus, ELF hiss, and electromagnetic ion cyclotron waves. *Journal of Geophysical Research*, *112*, A04207. https://doi.org/10.1029/2006JA011993

Summers, D., Thorne, R. M., & Xiao, F. L. (1998). Relativistic theory of wave-particle resonant diffusion with application to electron acceleration in the magnetosphere. *Journal of Geophysical Research*, *103*(A9), 20,487–20,500. https://doi.org/10.1029/98JA01740

Tao, X. (2014). A numerical study of chorus generation and the related variation of wave intensity using the DAWN code. *Journal of Geophysical Research: Space Physics*, *119*, 3362–3372. https://doi.org/10.1002/2014JA019820

Taubenschuss, U., Santolik, O., Breuillard, H., Li, W., & le Contel, O. (2016). Poynting vector and wave vector directions of equatorial chorus. *Journal of Geophysical Research: Space Physics*, *121*, 11,912–11,928. https://doi.org/10.1002/2016JA023389

Teng, S. C., Tao, X., Li, W., Qi, Y., Gao, X. L., Lei, D., et al. (2018). A statistical study of the spatial distribution and source-region size of chorus waves using Van Allen Probes data. *Annales de Geophysique*, *36*(3), 867–878. https://doi.org/10.5194/angeo-36-867-2018

Thorne, R. M. (2010). Radiation belt dynamics: The importance of wave-particle interactions. *Geophysical Research Letters*, *37*, L22107. https://doi.org/10.1029/2010GL044990

Thorne, R. M., Li, W., Ni, B., Ma, Q., Bortnik, J., Chen, L., et al. (2013). Rapid local acceleration of relativistic radiation-belt electrons by magnetospheric chorus. *Nature*, *504*(7480), 411–414. https://doi.org/10.1038/nature12889

Thorne, R. M., Ni, B., Tao, X., Horne, R. B., & Meredith, N. P. (2010). Scattering by chorus wave as the dominant cause of diffuse auroral precipitation. *Nature*, *467*(7318), 943–946. https://doi.org/10.1038/nature09467

Thorne, R. M., O'Brien, T. P., Shprits, Y. Y., Summers, D., & Horne, R. B. (2005). Timescale for MeV electron microburst loss during geomagnetic storms, *Journal of Geophysical Research*, *110*, A09202, doi:https://doi.org/10.1029/2004JA010882.

Tsurutani, B. T., & Smith, E. J. (1974). Postmidnight chorus: A substorm phenomenon. *Journal of Geophysical Research*, *79*(1), 118–127. https://doi.org/10.1029/JA079i001p00118

Tsurutani, B. T., & Smith, E. J. (1977). Two types of magnetospheric ELF chorus and their substorm dependences. *Journal of Geophysical Research*, *82*(32), 5112–5128. https://doi.org/10.1029/JA082i032p05112

Wu, S., Denton, R. E., Liu, K., & Hudson, M. K. (2015). One- and two-dimensional hybrid simulations of whistler mode waves in a dipole field. *Journal of Geophysical Research: Space Physics*, *120*, 1908–1923. https://doi.org/10.1002/2014JA020736

Xiao, F. L., Su, Z. P., Zheng, H. N., & Wang, S. (2009). Modeling of outer radiation belt electron by multidimensional diffusion process. *Journal of Geophysical Research*, *114*, A03201. https://doi.org/10.1029/2008JA013580